Paleoceanography and Paleoclimatology

RESEARCH ARTICLE
10.1029/2023PA004732

Key Points:

- A drier mid-Holocene and wetter late-Holocene occurred in Red River catchment controlled by the shift of Western Pacific Subtropical High
- A decoupling between chemical weathering in Red River catchment and summer monsoon was caused by shelf exposure during the deglaciation
- The relative content of magnetofossils in northwestern South China Sea is controlled by the sea level and deep-water environment changes

Supporting Information:

Supporting Information may be found in the online version of this article.

Correspondence to:

Z. Jiang,
jiangzhaoxia@ouc.edu.cn

Citation:

Sun, Q., Jiang, Z., Xiao, C., Chen, L., Liu, W., He, K., et al. (2024). Magnetic fingerprints for the paleoenvironmental evolutions since the last deglaciation: Evidence from the northwestern South China Sea sediments. *Paleoceanography and Paleoclimatology*, *39*, e2023PA004732. https://doi.org/10.1029/2023PA004732

Received 29 JULY 2023
Accepted 24 FEB 2024

Author Contributions:

Conceptualization: Qishun Sun, Zhaoxia Jiang, Chunfeng Xiao, Long Chen, Yulong Guan, Yuzhen Zhang, Sanzhong Li
Data curation: Qishun Sun
Formal analysis: Kuang He, Haosen Wang
Funding acquisition: Zhaoxia Jiang
Investigation: Qishun Sun, Wanxin Liu
Methodology: Qishun Sun, Zhaoxia Jiang, Chunfeng Xiao, Long Chen, Wanxin Liu, Kuang He, Yulong Guan, Yuzhen Zhang, Haosen Wang
Project administration: Zhaoxia Jiang
Resources: Liang Chen, Zhengxin Yin
Validation: Qishun Sun, Zhaoxia Jiang
Visualization: Qishun Sun
Writing – original draft: Qishun Sun
Writing – review & editing: Zhaoxia Jiang

Magnetic Fingerprints for the Paleoenvironmental Evolutions Since the Last Deglaciation: Evidence From the Northwestern South China Sea Sediments

Qishun Sun[1], Zhaoxia Jiang[1,2], Chunfeng Xiao[1], Long Chen[1], Wanxin Liu[1], Kuang He[1,2], Yulong Guan[1], Yuzhen Zhang[1], Haosen Wang[3], Liang Chen[4], Zhengxin Yin[4], and Sanzhong Li[1,2]

[1]Frontiers Science Center for Deep Ocean Multispheres and Earth System, Key Laboratory of Submarine Geosciences and Prospecting Techniques, Ministry of Education, Chongben Honors College, College of Marine Geosciences, Ocean University of China, Qingdao, PR China, [2]Laboratory for Marine Geology, and Laboratory for Marine Mineral Resources, Laoshan National Laboratory, Qingdao, PR China, [3]Center for Marine Magnetism (CM^2), Department of Ocean Science and Engineering, Southern University of Science and Technology, Shenzhen, PR China, [4]South China Sea Marine Survey and Technology Center, State Oceanic Administration, Guangzhou, China

Abstract Rapid global changes since the last deglaciation can be well documented in marginal sea sediments, while isolating individual paleoenvironmental signals is still challenging. Here, we identified magnetic minerals and unmixed their variations in sediments from the northwestern South China Sea to decipher environmental variations since the last deglaciation. The variation in the hematite to goethite ratio indicates a relatively drier mid-Holocene and a wetter early and late Holocene in the Red River catchment. The position shift and intensity variation of Western Pacific Subtropical High may account for the Holocene precipitation changes. A higher chemical weathering intensity accompanied by a relatively more fine-grained magnetite input during the last deglaciation suggests decoupling of the Asian Summer Monsoon and chemical weathering in the catchment, which might have been caused by the shelf exposure during the deglaciation. In addition, the relative abundance of biogenic magnetite increased with the sea level and possible deep-water temperature rise. Therefore, magnetic minerals such as hematite, goethite, detrital and biogenic magnetite are markedly potential fingerprints for continent-ocean environmental changes.

Plain Language Summary The global climate, which has changed rapidly since the last deglaciation, has been recorded by marginal sea sediments. However, the mixing of environmental factors renders it difficult to isolate individual information. Here, we unmixed the magnetic mineralogical signals of sediments from the northwestern South China Sea since the last deglaciation. We found that a higher hematite to goethite ratio (Hm/Gt) in our core represents higher precipitation in Red River catchment. The Hm/Gt variation indicates a relatively drier mid-Holocene and a wetter early and late-Holocene in the Red River catchment, which is consistent with the precipitation records in Southern China but opposite to that of Northern China. The chemical weathering of the Red River catchment was decoupled from the Asian Summer Monsoon, exhibiting a higher weathering extent (more fine-grained magnetite was generated) during the last deglaciation due to secondary weathering on the continental shelf. Moreover, the relative abundance of magnetofossils in our core was consistent with changes of the sea level and deep-water environments. Therefore, the isolation of magnetic mineral information from marginal sea sediments can help to reconstruct the continent-ocean environmental changes.

1. Introduction

The last deglaciation to Holocene is a typical cold and warm transition period, accompanied by the rapid rise of atmospheric CO_2 concentration and sea level (e.g., Clark et al., 2012; Lambeck et al., 2014), surface and bottom current interchanges (e.g., Wan & Jian, 2014; Zheng et al., 2016), and the occurrence of millennial-scale climate events, known as Bølling-Allerød (BA) and Younger Dryas (YD) events (Clark et al., 2012). Marginal sea is one of the most sensitive regions to these global changes (e.g., Liu et al., 2016; Zhong et al., 2021). However, the complex source-to-sink processes in marginal seas make it challenging to effectively extract climate, continental weathering, and marine environment signals from sediments, even for the widely studied last deglaciation and Holocene periods (Kissel et al., 2020). Therefore, the understanding of the paleoclimate, paleoenvironment, and chemical weathering remains in dispute for marginal sea sediments.

The South China Sea (SCS) is the largest marginal sea separating the Asian continent from the Pacific, with a large fluvial input from the surrounding continent and islands; therefore, it is an excellent area for reconstructing the paleoclimate (e.g., East Asian monsoon evolution) and weathering history in the source area (Liu et al., 2016). Nevertheless, Holocene precipitation records for the northwestern SCS and its surrounding areas remain controversial. Both the precipitation records in the northwestern SCS (Li et al., 2022) and the upper reaches of the Red River (Chen et al., 2014) reveal a decreasing trend in precipitation after the early Holocene, while the records from the southwestern China support a relatively wet late Holocene and a distinctly arid mid-Holocene (Xu et al., 2020). Thus, more records are needed to reconstruct the precipitation changes in the Red River catchment and its surrounding areas. In addition, the influence of northwestern SCS shelf exposure and inundation caused by sea-level variations should also be further considered, in particular on fluvial chemical weathering records since the last deglaciation, because it may overwhelm the continental weathering response to climate change (Wan et al., 2017).

Magnetic mineralogy has been widely used to infer different paleoclimatic and paleoenvironmental records of marine and terrestrial sediments (e.g., Ao et al., 2020; Kissel et al., 2020; Zhong et al., 2021). For example, the relative contents of hematite and goethite have been used to indicate arid/humid conditions in source/sink areas, such as, the Chinese Loess Plateau and SCS (e.g., Ao et al., 2020; Jiang et al., 2022; Zhang et al., 2007). The concentrations of fine-grained magnetite and maghemite can indicate the intensity of pedogenesis induced by the summer monsoon in Chinese loess/paleosols (e.g., Liu et al., 2004; Zhou et al., 1990). However, magnetic minerals in marginal sea sediments are usually well mixed, for example, a mixture of low-coercivity detrital and biogenic magnetite (magnetofossils) (e.g., Chang et al., 2016; Wang, Xu, et al., 2022) with high-coercivity hematite and goethite (e.g., Jiang et al., 2022; Zhang et al., 2007). Thus, these magnetic minerals should be identified and separated first, especially for the northwestern SCS sediments affected by various source-to-sink processes, and then used to reconstruct the paleoenvironments of the marginal seas and the adjacent continents.

The Qiongdongnan basin is an ideal area for exploring the continent-ocean changes since the last deglaciation, owing to the relatively simple and continuous sediment supply from the Red River catchment (Figure 1) (Li et al., 2022; Wan et al., 2015; Xiao et al., 2023). Here, we unmixed the magnetic mineralogy records using magnetic methods and diffuse reflectance spectroscopy (DRS) measurements, where the latter is effective for the identification and semi-quantification of hematite and goethite (e.g., Jiang et al., 2022). Precipitation, chemical weathering, and deep-sea environmental changes since the last deglaciation were reconstructed based on these magnetic proxies.

2. Regional Settings

The SCS receives more than 700 million metric tons (Mt) of fluvial sediments annually, including those from several of the world's largest rivers, such as the Mekong, Red, and Pearl Rivers (Figure 1a) (Liu et al., 2016). In the northwestern SCS, the Qiongdongnan basin primarily accumulates terrestrial sediments from the Red River (Figure 1b) (Li et al., 2022; Wan et al., 2015; Xiao et al., 2023). The upper reaches of the Red River catchment are characterized by the prevalent presence of red soils that are significantly eroded by tectonic activities and sufficient runoff (Le et al., 2007), while the delta region (Figure 1b) of the Red River is dominated by gray and alluvial soils (Le et al., 2007).

Terrestrial sediments transported to the Beibu Gulf can be discharged into the Qiongdongnan basin by surface currents (Figure 1b) (Gao et al., 2017; Tian et al., 2020). Since the last deglaciation, changes in sea level have substantially influenced the configuration of the land and sea in the northwestern SCS (Figure S1 in Supporting Information S1). Simulated shoreline changes in the northwestern SCS indicate that the Beibu Gulf and the Yinggehai basin were exposed between 20 and 15 ka BP (Figures S1a and S1b in Supporting Information S1). The exposed shelf served as a bridge connecting the Hainan Island, the Annamite Mountain Range, and South China. The Paleo-Red River catchment was formed during this period. Sea levels raised rapidly and submerged the exposed shelf between 15 and 10 ka BP, ultimately resulting in the formation of a modern-like Red River catchment at 10 ka BP (Figure S1c in Supporting Information S1). Since 10 ka BP, no significant shoreline changes have occurred except for a minor shoreline recession (Figure S1d in Supporting Information S1). To avoid confusion, both modern-like Red River catchment and paleo-Red River catchment are termed as "Red River catchment" uniformly.

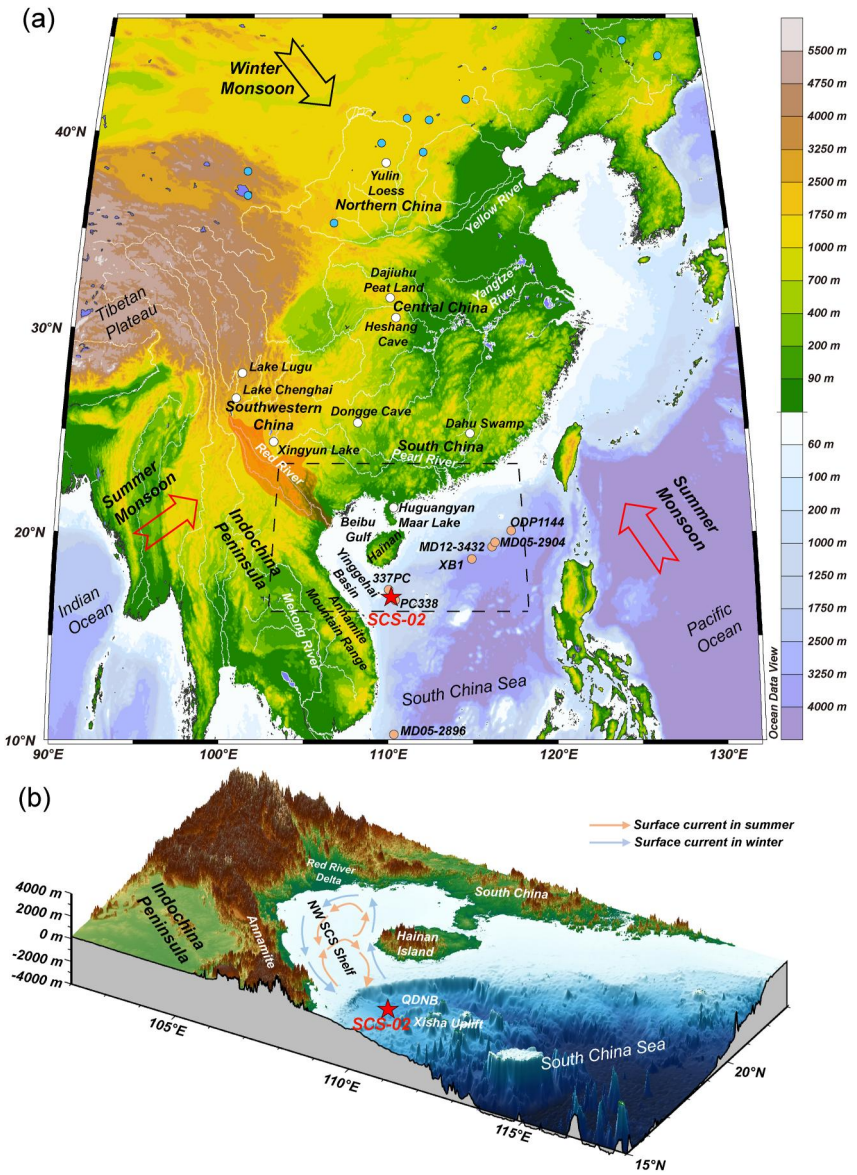

Figure 1. Geographic and topographic settings of northwestern South China Sea (SCS). (a) Regional map showing the position of core SCS-02 (red star) and other referenced sites in South China Sea (orange dots) (Chen et al., 2017; Hu et al., 2012; Li et al., 2022; Wan et al., 2015; Wan & Jian, 2014; Wang, Xu, et al., 2022). The white and blue dots indicate the positions of continental records, where the blue dots are fossil pollen sites from northern China (Li, Yan, et al., 2018). The Red River catchment is marked with orange shading. (b) Topographic map of northwestern SCS. The core SCS-02 is marked with red star and the regional surface circulations (Gao et al., 2017) are marked with arrows. The QDNB represents Qiongdongnan basin.

3. Materials and Methods

3.1. Materials

The studied gravity core SCS-02 (16.77°N, 110.30°E; length of 2.54 m), located in the Qiongdongnan basin in the northwestern SCS with a water depth of 1,400 m (Figure 1), was cored by the SCS Marine Survey and Technology Center, Ministry of Natural Resources in 2019 using "Haice 3301" vessel. The gravity core was separated into two halves, one for the study and the other for archive. Along the central axis of the first half, 127 samples were retrieved using $2 \times 2 \times 2$ cm^3 plastic cubes sequentially. In addition, unoriented wet samples were collected from the same locations as the cubic samples and freeze-dried for geochemical, DRS, and rock magnetic

measurements. The sediment was primarily composed of clayey silt without any visible coring disturbance. The age model for core SCS-02 was constrained by five AMS ^{14}C dates for planktonic foraminifera (Figure S2 and Table S1 in Supporting Information S1) (Xiao et al., 2023).

3.2. Magnetic Measurements

A series of environmental magnetic measurements was conducted on all 127 samples. The magnetic susceptibility of low- (χ_{lf}, 967 Hz) and high- (χ_{hf}, 15,616 Hz) frequencies were measured using a Kappabridge MFK1-FA. The percentage of frequency-dependent susceptibility (χ_{fd}%) was calculated as $\chi_{fd}\% = (\chi_{lf} - \chi_{hf})/\chi_{lf} \times 100\%$. The anhysteretic remanant magnetization (ARM) was imparted in a peak alternating field (AF) of 80 mT with a direct current (DC) bias field of 0.05 mT using a 2G Enterprises superconducting magnetometer. The values of χ_{ARM} was calculated by normalizing ARM with the applied DC bias field. Isothermal remanent magnetization (IRM) was imparted by a pulse magnetizer (ASC Scientific, USA) and then measured in the 2G Enterprises superconducting magnetometer. We defined the IRM obtained at 1 T as saturated isothermal remanence (SIRM) and IRM_{-300mT} obtained at a reversed field of 300 mT. The "hard" IRM (HIRM) and S-ratio is defined as $0.5 \times (SIRM + IRM_{-300mT})$ and $-IRM_{-300mT}/SIRM$ (King & Channell, 1991), respectively. Hysteresis loops were measured under the maximum applied field of 1 T using a Lake Shore 8604 vibrating sample magnetometer (VSM 8604). Subsequently, IRM was imparted to samples in a 1 T field, which was demagnetized in a stepwise back-field to obtain the coercivity of remanence (B_{cr}).

The first-order reversal curves (FORCs) were obtained for 20 representative freeze-dried samples with VSM 8604, which were then processed using software *FORCinel* (version 3.06) to perform principal component analysis (FORC-PCA) for unmixing distinct magnetic minerals (Harrison et al., 2018; Harrison & Feinberg, 2008; Lascu et al., 2015). Low-temperature SIRM (maximum field of 2.5 T) warming curves were measured from 10 to 300 K for 10 representative samples after zero field cooling (ZFC) with a Magnetic Property Measurement System (MPMS-3).

3.3. Non-Magnetic Measurements

3.3.1. TEM Analysis

To determine the morphologies of these magnetic particles, transmission electron microscopy (TEM) observation was conducted using a HITACHI HT770 TEM operating at 100 kV for the magnetic extracts from 10 representative samples following the procedure of He and Pan (2020).

3.3.2. Major and Trace Element Measurement

A total of 88 freeze-dried samples with 2- to 4-cm sample intervals were ground into powder and subjected to major and trace elemental analyses using Inductively Coupled Plasma Optical Emission Spectrometry (ICP-OES) and Inductively Coupled Plasma Mass Spectrometry (ICP-MS), respectively. Approximately 40 mg powder for each sample was placed into steel-jacketed bombs and digested in a mixture of HF and HNO_3 in the oven at 195°C for 3 days. Following the cooling phase, the solution was dried on a hotplate, and reconstituted with 5 ml of a 15wt% HNO_3 solution and 1 ml of the Rh internal standard. Subsequently, they were resealed and heated at 150°C overnight. Then, an aliquot of the digestion was diluted and atomized into ICP-OES and ICP-MS to measure the major contents (except elemental Si) and trace elements, respectively. For elemental Si determination, approximately 30 mg of the sample was needed for alkali fusion before being introduced into the ICP-OES. The Chemical Index of Alteration (CIA) and K/Al ratios can represent the extent of chemical weathering of samples, which is based on the relative mobility of Na, K, and Ca in aqueous fluids and the relative immobility of Al (Nesbitt & Young, 1982). The CIA was calculated as follows: $CIA = Al_2O_3/(Al_2O_3 + CaO^* + Na_2O + K_2O) \times 100\%$. The CaO* value represents the CaO content in the silicate fraction of the sediment and was acquired using the method as described in McLennan (1993). The principal component analysis (PCA) of the major elements was conducted using IBM SPSS Statistics 19 software to extract combinations of variables that were correlated with the relationships among elements/oxides (Huang et al., 2016; Li et al., 2022).

3.3.3. DRS Measurement

Diffuse reflectance spectroscopy (DRS) measurements were performed on all samples using an ultraviolet-visible-infrared spectrometer (Cary 5000) equipped with $BaSO_4$ as a white standard. DRS data were substituted into the Kubelka–Munk (K–M) remission function ($F(R) = (1 - R)^2/2R$, where R is the reflectance) (Scheinost et al., 1998). The first- and second-derivative curves of F(R) were calculated. The second-derivative curve was used to obtain the band intensities of hematite (I_{Hm}) and goethite (I_{Gt}), which were proportional to the concentration of hematite and goethite, respectively (Scheinost et al., 1998; Torrent et al., 2007). The band ranges of hematite and goethite should be approximately 535 and 425 nm, respectively. The I_{Hm}/I_{Gt}, defined as Hm/Gt, can be used as a proxy for the relative abundances of these two minerals (e.g., Jiang et al., 2022).

4. Results

4.1. Identification of Magnetic Minerals

The low-temperature SIRM warming curves showed a pronounced remanence decrease at 100–120 K for all measured samples owing to the Verwey transition (Figure 2a). The first-derivative curves revealed two distinct peaks at ∼100 and ∼120 K (Figure 2b), which may indicate the existence of biogenic and detrital magnetite, respectively (Chang et al., 2016). Both peaks were obvious for the samples after 13.2 ka BP, while only one peak (∼120 K) was well-observed for samples before 13.2 ka BP (Figure 2b). The FORCs of typical samples contained a major central ridge component along $B_u = 0$ (Figure 2c), which is a typical characteristic of biogenic magnetite. The weak longitudinal distribution of FORCs may be caused by the presence of collapsed magnetosome chains and detrital magnetic minerals (Chang et al., 2018). Needle-shaped (giant magnetofossil size, >1,100 nm in our observation) and bullet-shaped, cubo-octahedral magnetite particles in chain were observed in the TEM (Figure 2d), which provides direct evidences for the occurrence of magnetofossils.

The FORC-PCA results can further constrain the relative contents of detrital and biogenic magnetite (Lascu et al., 2015). The FORC diagram of endmember 1 (EM1) shows a significant vertical spread (Figure 2f), which is a characteristic of interacting single domain (SD) or detrital vortex state grains (Roberts et al., 2000, 2018). The elliptical peak and the peak close to the origin of the FORC diagram also indicated the occurrence of SD and superparamagnetic (SP) grains (Pike et al., 2001; Yamazaki et al., 2020), respectively. The endmember 2 (EM2) has a pronounced central ridge (Figure 2g) that presents the non-interacting SD particles (Egli et al., 2010). Temporal variations in EM1 (detrital magnetite) and EM2 (biogenic magnetite) (Figures 2h and 2i) showed that the relative contribution of biogenic magnetite increased since 13.2 ka BP, consistent with the low-temperature results.

The second-derivative curves of DRS showed that both hematite and goethite existed in the sediment (Figure S3 in Supporting Information S1), with average characteristic peaks at 543.6 and 420.3 nm, respectively. The S-ratio has been above 0.9 since 15 ka BP (Figure S4b in Supporting Information S1), therefore, the magnetic remanence is dominated by magnetite.

4.2. Major and Trace Elements Results

The major elements of the samples consisted mainly of Al_2O_3, TiO_2, TFe_2O_3, SiO_2 and K_2O, and their temporal variation trends were analogous to each other, while they were opposite to CaO (Figure 3). They decreased gradually as sea level rose during the last deglaciation, increased during ∼12–9 ka BP, peaked at approximately 9 ka BP, and then decreased to a relatively stable value after 9 ka BP. The first principal component (PC1) explained 61.4% of the variance within the major element data set and mainly contains the aforementioned elements which are usually considered to be more resistant and insoluble (Figure S6 in Supporting Information S1). In contrast, the other major elements (e.g., CaO and Na_2O), which were relatively soluble and mobile, showed negative loadings on PC1 (Figures S5 and S6 in Supporting Information S1). The CIA was consistent with the K/Al (Figures 3i and 3j), showed a relatively higher chemical alteration during deglaciation than during the Holocene. The enrichment factors (EF) of the redox-sensitive elements Mo and U were calculated as $X_{EF} = [(X/Al)_{sample}/(X/Al)_{PAAS}]$ (where PAAS is the Post Archean Australian Shale and X and Al represent the weight concentrations of elements X and Al, respectively) (Algeo & Tribovillard, 2009). Mo_{EF} and U_{EF} exhibited similar patterns in core SCS-02, showing higher values during deglaciation and a decreasing trend during the Holocene (Figure S7 in Supporting Information S1).

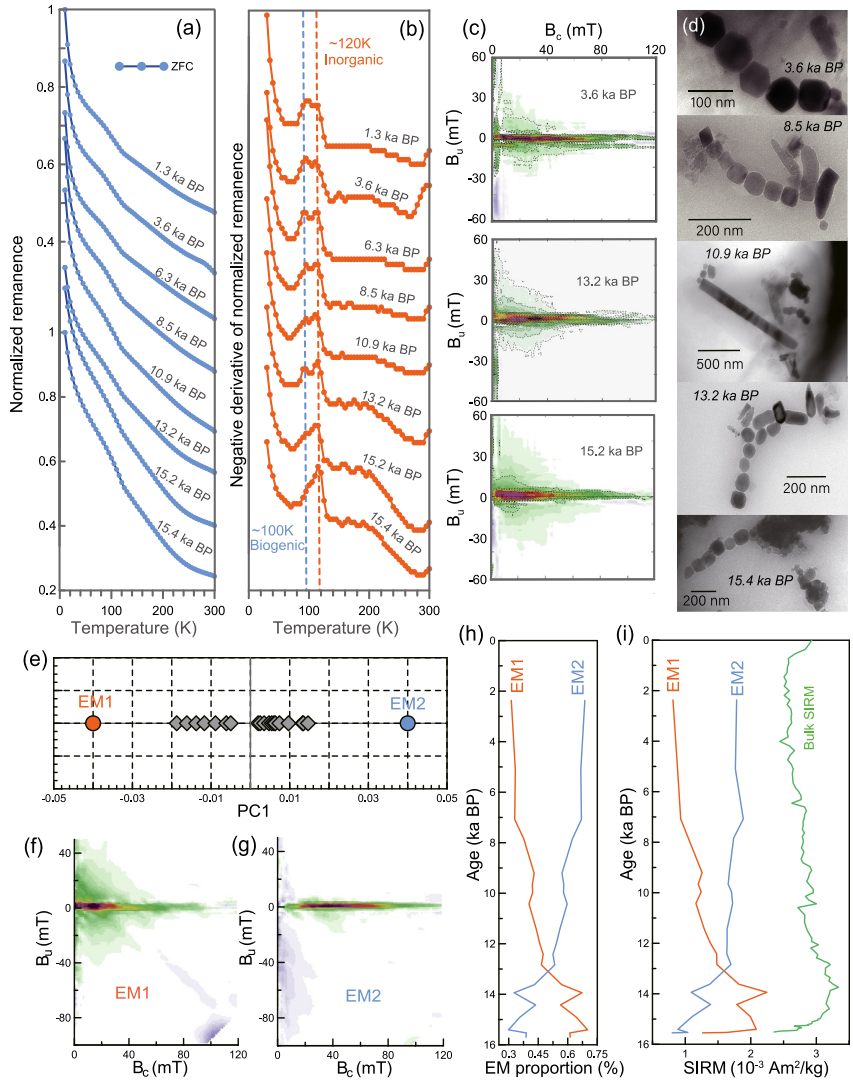

Figure 2. Identification of different magnetite types in core SCS-02 and FORC-PCA results. (a) Low-temperature SIRM warming curves after zero field cooling (ZFC) treatment for representative samples. All data was normalized by the SIRM values at 10 K. (b) The negative derivatives of the ZFC curves. The vertical dashed lines indicate the two peaks at ~100 and ~120 K, respectively. (c) FORC diagrams for representive samples. (d) Transmission electron microscopy images of magnetofossils for selected samples. (e–i) The results of FORC-PCA. (e) PC1 score plot with two end-members (EM1 and EM2). (f–g) The FORC diagrams for EM1 and EM2, respectively. (h) The temporal variation of EM1 and EM2 proportion. (i) Bulk SIRM and the contributions to SIRM of individual EMs calculated from their respective proportions.

5. Discussion

5.1. Hm/Gt Ratio: An Effective Precipitation Proxy for the Source Area

The Red River catchment is the dominant sediment provenance for the Qiongdongnan basin (Figures 1a and 1b), as evidenced by the Sr-Nd isotopic characteristics of 337PC and PC338 from the Qiongdongnan basin (Li et al., 2022; Wan et al., 2015). In the Rare Earth index scatter plot (Figure S8 in Supporting Information S1) (Xiao et al., 2023), our samples are much closer to those reported for the Red River and Beibu Gulf samples, further indicating that the Red River is the main contributor to the study area. Moreover, magnetic property studies of Beibu Gulf sediments have shown that magnetic minerals can be discharged from the Red River into the Qiongdongnan basin (Figure 1b) (Tian et al., 2020).

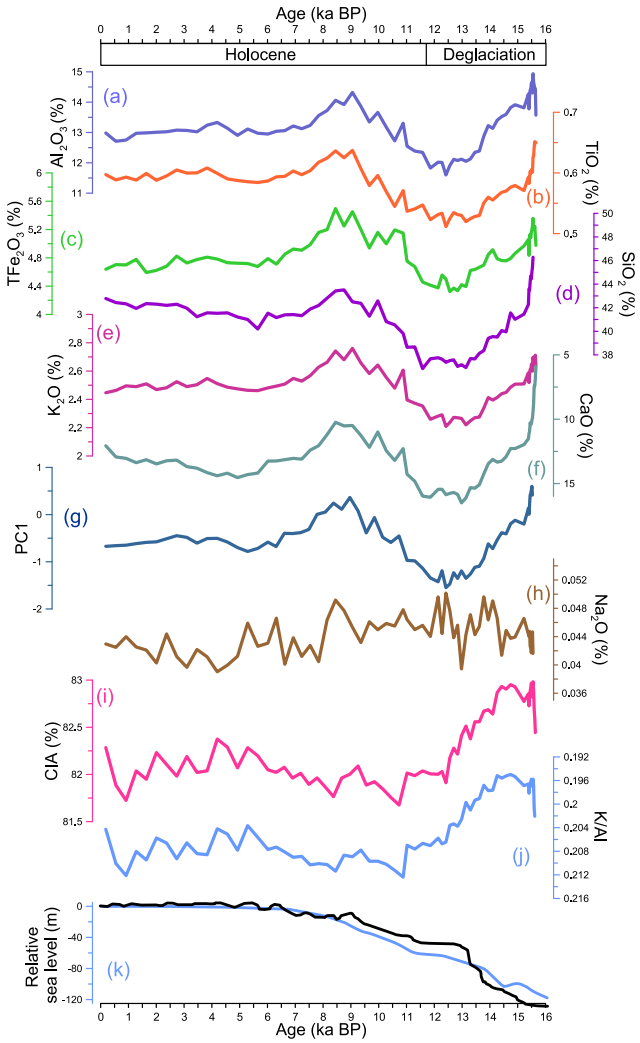

Figure 3. The relationship between major elements and the relative sea level. (a–f and h) The temporal variations of individual major element content. (g) PC1 from the results of principal component analysis of major elements. (i) Chemical Index of Alteration. (j) K/Al. (k) global (blue line) and northwestern South China Sea (black line) sea-level curves (Lambeck et al., 2014; Yao et al., 2009).

In general, the hematite-to-goethite ratio (Hm/Gt) is used to reflect the aridity/humidity degree of sink or source areas because of the opposite formation conditions (dry and warm for hematite, wet and cool for goethite) and competitive formation processes (e.g., Jiang et al., 2022; Schwertmann, 1993; Zhang et al., 2007). Therefore, a higher Hm/Gt value usually suggests drier climate conditions, whereas a lower Hm/Gt value indicates wetter conditions (e.g., Jiang et al., 2022; Lepre & Olsen, 2021). Representatively, Hm/Gt derived from southern SCS sediments has reconstructed the precipitation history of the Mekong River catchment over the last 600 ka, which is anti-correlated with ASM precipitation (Zhang et al., 2007). However, our Hm/Gt record (Figure 4a) is positively correlated with the ASM precipitation records from South China (e.g., Ti contents from the Huguangyan Maar Lake, humification degree from the Dahu swamp in the Nanling Mountains) (Figures 4c and 4d) (Yancheva et al., 2007; Zhong et al., 2010), Southwestern China (e.g., lake level of Lake Chenghai, and pollen concentration from Lake Lugu) (Figures 4e and 4f) (Xu et al., 2020; Zhang et al., 2018), and Central China (e.g., hopanoids content from the Dajiuhu Peatland, and $IRM_{soft\text{-}flux}$ of the Heshang Cave stalagmite) (Figures 4g and 4h) (Xie et al., 2013; Zhu et al., 2017) during Holocene. In addition, Hm/Gt was positively correlated with PC1 (Figure 4b) derived from the PCA of major elements during the Holocene, indicating that more hematite input was accompanied by an increase in relative insoluble and resistant elements. Thus, Hm/Gt was correlated with the discharge ability of the Red River during the Holocene. However, the deglacial records might have been affected by sea level changes (Figures 3g and 3k), thus we focused on the changes in Hm/Gt and PC1 during the Holocene.

The upper reaches of the Red River catchment with high erosion rates, are predominantly covered by hematite-rich red soils (Le et al., 2007; Nguyen et al., 2016), which serve as the primary source of hematite particles in the Red River and are responsible for the water color of Red River (Kissel et al., 2016; Nguyen et al., 2016). High precipitation may accelerate erosion of the upper reaches and scour more red soils into the Red River, reinforcing the relatively higher Hm/Gt ratio. However, the relationship between the Hm/Gt ratio and precipitation is not invariable due to mineral dissolution with high precipitation (Abrajevitch & Kodama, 2011; Balsam et al., 2004; Long et al., 2016). The relative concentration of goethite in the surface soil of southwest China, from which Red River origins, shows a linear negative correlation with precipitation owing to the dissolution of goethite with high precipitation (Zhang, Yang, et al., 2023). In contrast, hematite is more resistant to dissolution than goethite (Abrajevitch & Kodama, 2011). Consequently, Hm/Gt is an effective precipitation proxy for the study area, with a high value for strong precipitation.

In particular, the precipitation record in the Red River catchment during the Holocene can be divided into three stages: an evident wetting period (early Holocene, EH; ~11.5–7.5 ka BP), a dry interval (mid-Holocene, MH; ~7.5–4 ka BP), and a relative wetting period (late-Holocene, LH; after ~4 ka BP). Fluctuations of the monsoon precipitation during the Holocene are thought to be dominated by the orbital-scale summer insolation variations (Dykoski et al., 2005; Haug et al., 2001). Intense boreal summer insolation may lead to a northward shift of the intertropical convergence zone (ITCZ) (Haug et al., 2001) (Figures 4l and 4m) and subtropical summer monsoon fronts, resulting in enhanced precipitation. However, this may only refer to the precipitation record during the EH in the Red River catchment (Figure 5d). Our Hm/Gt record combined with the precipitation records from central and southern China suggest a drier environment during the MH and a relatively wetter hydroclimatic condition during the LH, which is inconsistent with the variation of the summer solar insolation (Figure 4m) (Berger & Loutre, 1991). In contrast, precipitation in Northern China reached a peak during the MH, based on the compiled

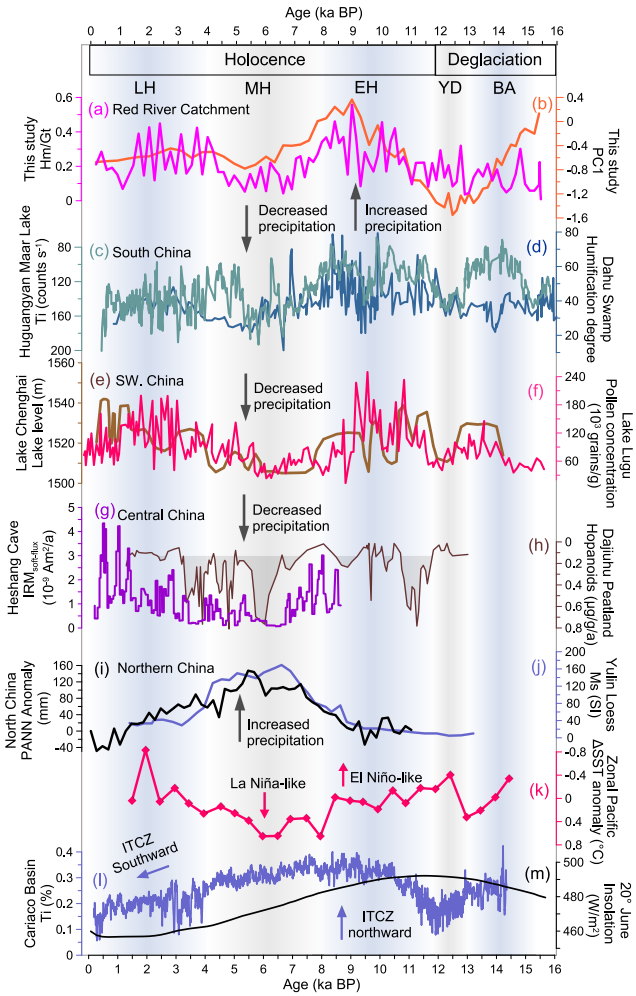

Figure 4. Precipitation records from core SCS-02 compared to other records: (a) hematite to goethite ratio of core SCS-02; (b) the first principal component (PC1) of principal component analysis for major elements of core SCS-02; (c) Ti content from Huguangyan Maar Lake (Yancheva et al., 2007); (d) humification degree from Dahu swamp (Zhong et al., 2010); (e) lake level curve of Lake Chenghai (Xu et al., 2020); (f) pollen concentration from Lake Lugu (Zhang et al., 2018); (g) stalagmite $IRM_{soft-flux}$ from Heshang Cave (Zhu et al., 2017); (h) mass accumulation rate of aerobic hopanoids in Dajiuhu peatland (Xie et al., 2013); (i) the regionally compiled anomaly record for Holocene annual mean precipitation (PANN) relative to its modern-day values in northern China (Li, Yan, et al., 2018); (j) magnetic susceptibility from Yulin loess section (Lu et al., 2013); (k) zonal Pacific ΔSST anomaly (Koutavas & Joanides, 2012); (l) Ti content from Cariaco basin (Haug et al., 2001); (m) 20°N June insolation (Berger & Loutre, 1991).

Holocene annual mean precipitation anomaly record in Northern China (Figures 1a and 4i) (Li, Yan, et al., 2018) and the precipitation proxy of the Yulin loess-paleosol section (Figure 4j) (Lu et al., 2013).

Recently, the juxtaposition of WPSH on the ASM has been interpreted as a key factor influencing East Asian precipitation (Liu et al., 2015; Rao et al., 2016; Xu et al., 2020). The maximum rainfall band in the East Asian region is located in the northwestern periphery of the WPSH (Rao et al., 2016), hence, the orbital-scale shift and intensity changes in WPSH may account for the observed uneven spatiotemporal distribution of precipitation from the Red River catchment to Northern China (Li, Yan, et al., 2018; Xu et al., 2020). The zonal tropical Pacific ΔSST anomaly changes (Figure 4k) (Koutavas & Joanides, 2012) may be the non-negligible factor modulating the location of WPSH (Rao et al., 2016; Xu et al., 2020). During the MH, the La Niña-like zonal Pacific ΔSST anomaly (Figures 4k and 5c) (Koutavas & Joanides, 2012), corresponding to a warmer western Pacific, would lead to intensified convective activity in the Philippines, which may drive the WPSH northward (Figure 5e) (Xu et al., 2020; Zhang, Smol, & Bu, 2023). Moreover, the amplification of the land-ocean thermal contrast between the northwestern Pacific and Northern China during this period might also have strengthened the WPSH (Figure 5e) (Li, Yan, et al., 2018). Therefore, the areas covering the Red River catchment to Central China were relatively arid during the MH because more water vapor was transported from the Indian Ocean and West Pacific to Northern China (Figure 5e). However, for the LH period, the southward movement of ITCZ (Figures 4l and 5f) (Haug et al., 2001) combined with the El Niño-like zonal Pacific ΔSST anomaly (Figure 4k) might induce the southward movement of WPSH through weakened Hadley circulation (Figure 5a), and cause the summer rain band shift southward (Figure 5f) (Xu et al., 2020; Zhang, Smol, & Bu, 2023).

5.2. Decoupling of Chemical Weathering and Asian Summer Monsoon Since the Last Deglaciation

As discussed above, the Red River catchment is the main sediment source for the study area. Thus, our CIA values (Figure 6e) can reflect the chemical weathering intensity of the Red River catchment. Strong chemical weathering may promote the formation of finer magnetic minerals related to pedogenesis processes (e.g., Liu et al., 2012; Su et al., 2015). Therefore, the concentration or grain size proxies for these finer magnetic minerals can indicate the pedogenesis and chemical weathering intensity (e.g., Hu et al., 2012; Su et al., 2015). SIRM is usually used to indicate the relative content of magnetic minerals, particularly SD magnetic minerals, while χ_{fd}% represents the magnetic particle input near the threshold of SD and superparamagnetic SP state (Liu et al., 2012; Thompson & Oldfield, 1986). EM1 from the FORC-PCA results shows the relative abundance of detrital magnetite (Figure 6c). The co-variation trends among the EM1, SIRM and χ_{fd}% indicated that SIRM and χ_{fd}% were mainly controlled by terrestrial magnetic mineral inputs rather than magnetofossils. According to the FORC diagrams of EM1 and EM2 (Figures 2f and 2g), the coercivity of detrital magnetite is lower than that of biogenic counterpart. Therefore, an increase of detrital magnetite can lead to a decrease in B_{cr} (Figure 6d). Our three magnetic parameters (SIRM, χ_{fd}%, and B_{cr}) coincided with the variation patterns of the CIA during the last deglaciation, indicating that more pedogenic magnetic minerals formed during chemical weathering processes. Therefore, these magnetic parameters are good indicators of the chemical weathering intensity over that period.

Our results suggest a strengthened chemical weathering during the deglacial period, especially during the BA event (Figures 6a–6f), when the summer monsoon intensified (Dykoski et al., 2005; Wang et al., 2016). By

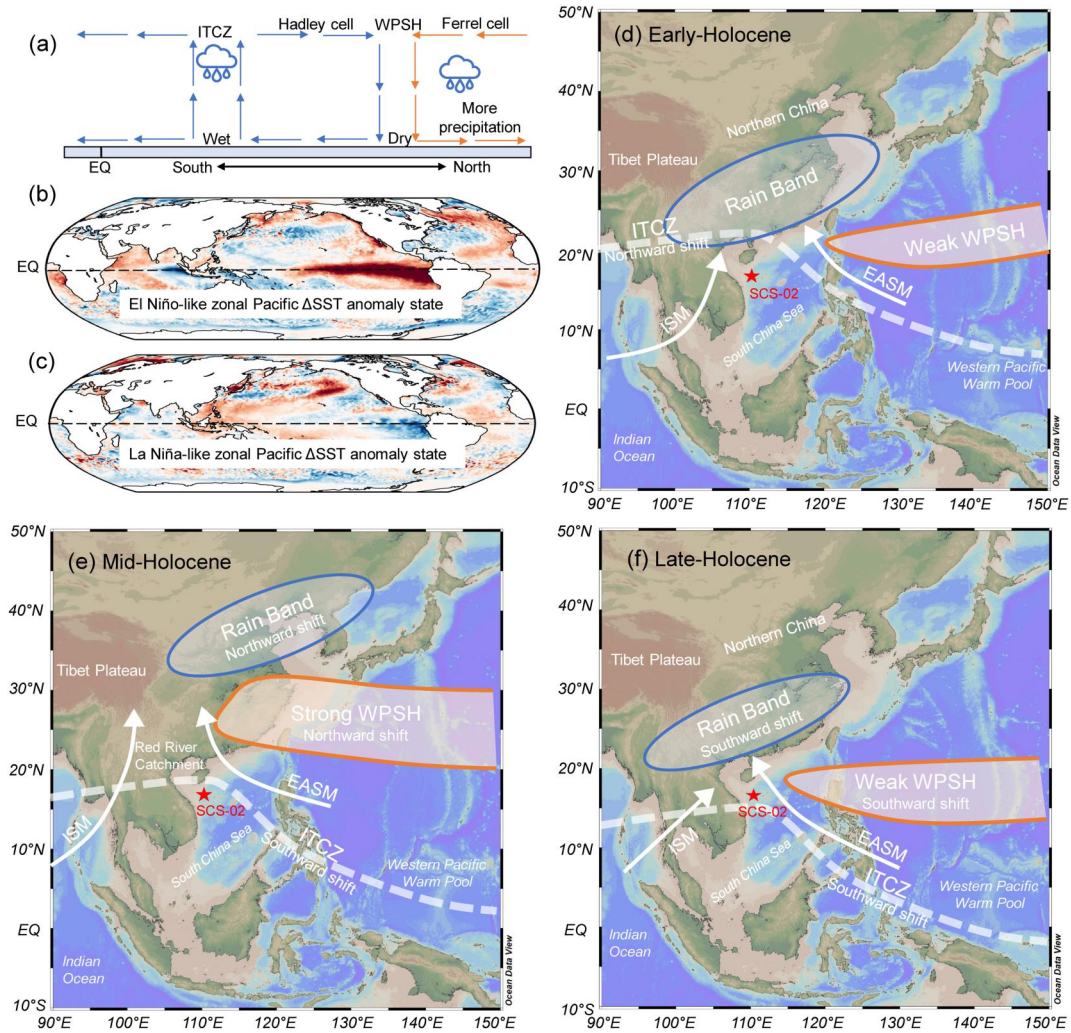

Figure 5. Schematic diagrams showing the possible mechanisms influencing the Holocene precipitation in the East Asia. (a) Models of atmospheric circulation in the middle and low latitudes of the Northern Hemisphere in summer (Zhang, Smol, & Bu, 2023). (b and c) The Pacific SST anomaly state during El Niño and La Niña, respectively. Sea surface temperature data from https://psl.noaa.gov/data/gridded/data.noaa.oisst.v2.highres.html. The La Niña SST anomaly in the figure was in 1997, and the El Niño SST anomaly was in 2013. (d and e) Schematic diagram of the mechanisms influencing the spatiotemporal precipitation allocation in the East Asia region over the Holocene. EASM: East Asian Summer Monsoon, ISM: Indian Summer Monsoon. The white dashed line shows the possible summer position of ITCZ. The red star showing the location of the core SCS-02 in this study.

contrast, the CIA and pedogenesis-related magnetic parameters (SIRM, χ_{fd}%, and B_{cr}) kept a relatively low state over the Holocene, the period with a stronger Asian summer monsoon and precipitation than the last deglaciation (Dykoski et al., 2005). Generally, the BA event and the EH (Holocene Optimum), are the two dominant wet periods after the Last Glacial Maximum in southern China (Dykoski et al., 2005; Wang et al., 2016). Precipitation in southern China was stronger during the EH than BA event (Figures 4c–4f). Moreover, the mean annual air temperature (MAAT) from the Huguangyan Maar Lake located at the same latitude to that of the Red River catchment (Figure 1a) showed a significant warming trend from BA event to EH (Figure 6h) (Li et al., 2023). These results suggest that ASM was stronger during EH than BA event (Figure 6g). Higher temperature and humidity often result in a stronger chemical weathering (West et al., 2005; White & Blum, 1995). Records from Southern China show that the CIA was higher during the EH than during the BA event (Wang, Zhong, et al., 2022). However, our CIA results indicates that the chemical weathering intensity was stronger during the BA event than during the EH (Figure 6e). Magnetic concentration parameters (e.g., χ, χ_{fd}% and SIRM) also displayed higher values in BA event. In particular, χ_{fd}% during the BA event (Figure 6b), a proxy of pedogenic

10.1029/2023PA004732

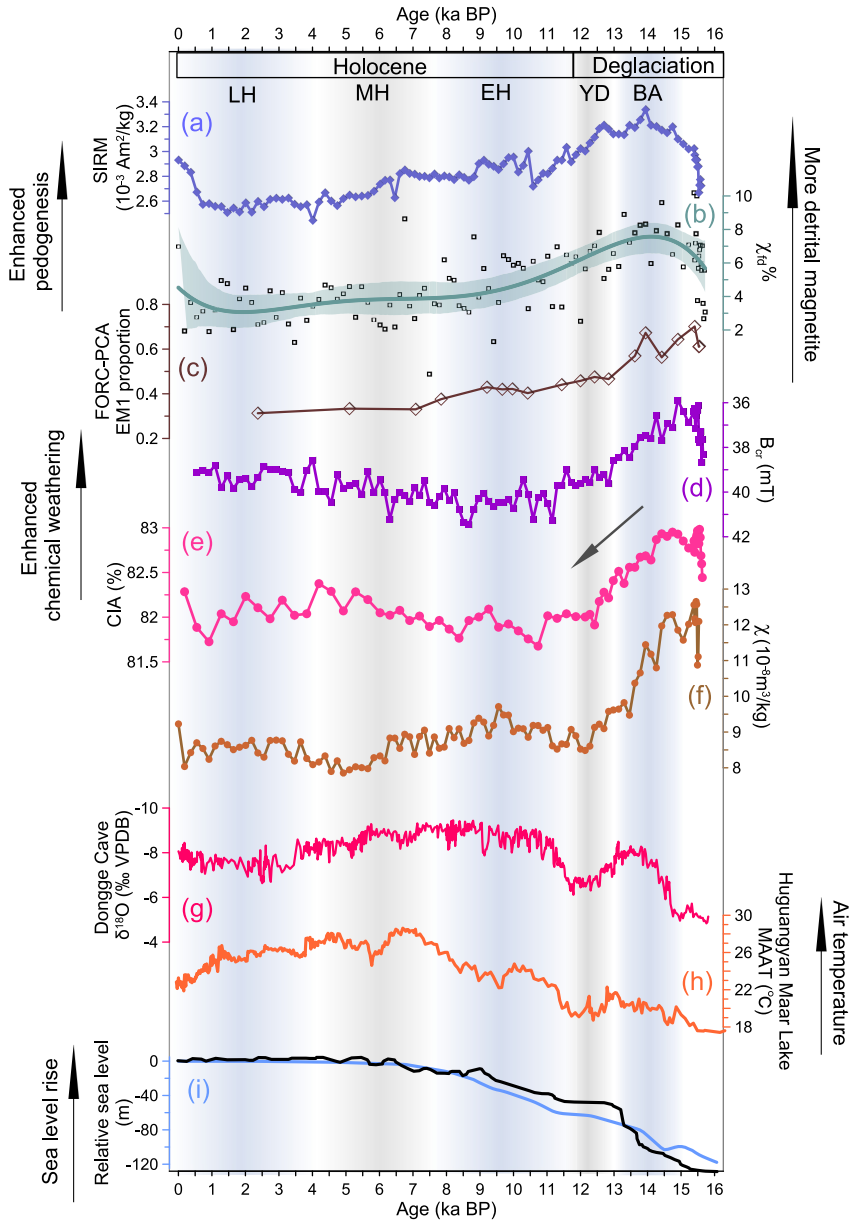

Figure 6. Weathering-related records from core SCS-02 compared to other records: (a) saturated isothermal remanence; (b) χ_{fd}%. The raw data (hollow squares), a quintic polynomial fit curve and the shading indicates 95% confidence level; (c) the EM1 proportion of first-order reversal curves principal component analysis results; (d) B_{cr}; (e) Chemical Index of Alteration; (f) χ; (g) stalagmite $\delta^{18}O$ records from Dongge Cave (Dykoski et al., 2005); (h) the mean annual air temperature from Huguangyan Maar Lake (Li et al., 2023); (i) relative sea level reconstructed for globe (blue line) (Lambeck et al., 2014) and northwestern SCS (black line) (Yao et al., 2009).

intensity in soils, was twice as high as that in the EH. Accordingly, the summer monsoon intensity cannot explain well the temporal variation in the chemical weathering records of the Red River catchment.

Continental chemical weathering is generally controlled by several factors such as tectonics, temperature, and humidity (Clift, 2006; Deng et al., 2022; White & Blum, 1995). For the northwestern SCS region, the influence of tectonics can be neglected at the millennium scale (Yao et al., 2009). Considering the significant glacial-interglacial sea level changes in the northwestern SCS (Figure S1 in Supporting Information S1) (Yao et al., 2009), the shelf sediments deposited during the interglacial periods were resuspended and redeposited into the lower slopes and basins during the subsequent low sea level periods, subjecting the shelf materials to

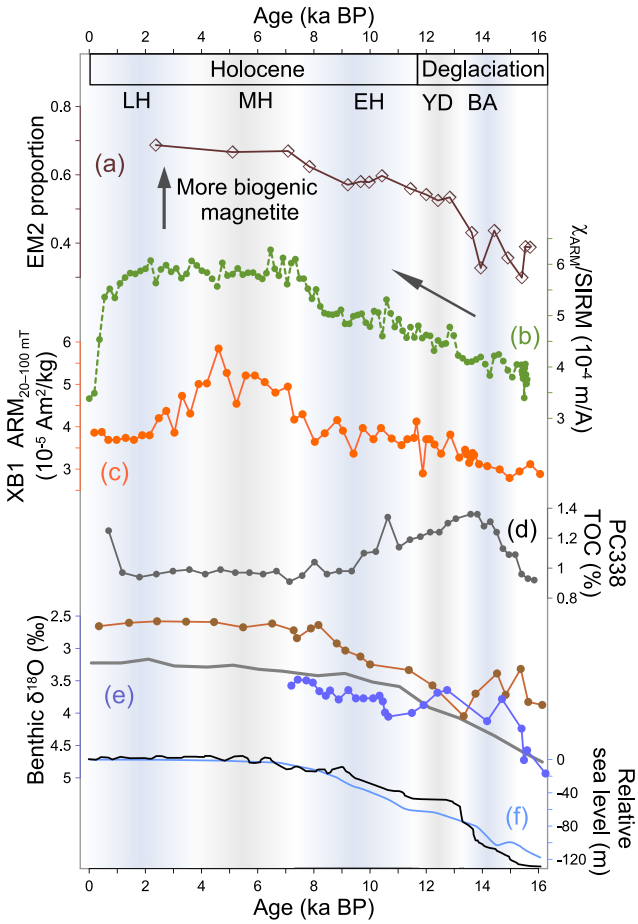

Figure 7. Biogenic magnetite-related proxies from core SCS-02 compared to other records: (a) the EM2 proportion of first-order reversal curves principal component analysis results; (b) χ_{ARM}/SIRM; (c) $ARM_{20–100mT}$ from core XB1 in northwest sub-basin of SCS (Wang, Xu, et al., 2022); (d) total organic carbon content from core PC338 in northwestern SCS (Li, Ouyang, et al., 2018); (e) benthic foraminiferal $\delta^{18}O$ data records. The gray curve represents the LR04 stack (Lisiecki & Raymo, 2005). The blue and red curves are from MD05-2904 located in the northern SCS (water depth of 2066 m) and MD05-2896 located in northern SCS (water depth of 1,657 m), respectively (Wan & Jian, 2014); (f) relative sea level reconstructed for globe (blue line) (Lambeck et al., 2014) and northwestern SCS (black line) (Yao et al., 2009).

composite weathering during interglacial sediment generation and after shelf exposure (Wan et al., 2017). Therefore, although a relatively cold and dry climate may suppress the rate of chemical weathering during glacial periods (White & Blum, 1995), the materials accommodated on the exposed shelf could be further weathered during their residence time (Hu et al., 2012; Wan et al., 2017). Thus, during the BA event, the relatively warm and humid climate further promoted the chemical weathering of materials on the wide exposed shelf. More pedogenic fine-grained and strongly magnetic minerals (e.g., magnetite) were generated during this process.

Additionally, the CIA decreased gradually as the coastline retreat during 14–11.5 ka BP and reached a minimum during Younger Dryas (YD) event with cold and dry climate (Figure 6e). The simulation result shows that the shoreline retreated and the northwestern SCS shelf was almost submerged at approximately 10 ka BP (Figure S1 in Supporting Information S1) (Yao et al., 2009), hence the materials on the continental shelf could not be further weathered, leading to a weaker chemical weathering record during the Holocene. Therefore, secondary weathering on the continental shelf during the low sea level period is the dominant reason for the decoupling of chemical weathering and the ASM.

5.3. Sea Level and Deep-Water Environment Control on the Relative Abundances of Magnetofossils

The monsoon precipitation and seal level variation since the last deglaciation may have influenced the terrestrial input and deep-water environment, particularly the nutrient supply, which may have affected the boom of magnetotactic bacteria (MTB) and the preservation of magnetofossils in Qiongdongnan basin (Roberts et al., 2011; Wang, Xu, et al., 2022).

Our FORC-PCA results show that biogenic magnetite was abundant during the MH and LH at higher sea level (Figure 7a). χ_{ARM}/SIRM has recently been used to determine the relative abundance of magnetofossils in sediments (Wang, Xu, et al., 2022; Yamazaki et al., 2020; Zhang et al., 2022), which showed that the relative abundance of magnetofossils increased gradually during the last deglaciation and reached a stable state during the MH and LH (Figures 7a and 7b). The relative variation in magnetofossil abundance in the Qiongdongnan basin was consistent with that in the northwest sub-basin of the SCS (Figure 7c) (Wang, Xu, et al., 2022). Combined with the absolute abundance of magnetofossils in core XB1 ($ARM_{20–100mT}$) (Figure 7c) (Wang, Xu, et al., 2022), we divided the temporal variation in magnetofossils in the northwestern SCS region into two stages. Stage 1 (the last deglaciation and EH) was characterized by a continuous increase in the relative abundance of magnetofossils, whereas Stage 2 (the MH and LH) was characterized by a stably high abundance of magnetofossils.

More organic carbon (Figure 7d) (Li, Ouyang, et al., 2018) and detrital iron oxide (Figure 6a) were transported into the Qiongdongnan basin during Stage 1 than during Stage 2, but less magnetofossils existed in Stage 1, which indicates that the nutrient supply was not the dominant factor for the different abundances of magnetofossils between Stage 1 and Stage 2. Instead, the magnetofossil concentration corresponded well to the sea level change (Figures 7a and 7f), so the sea level might affect the relative abundance of magnetofossils (Lambeck et al., 2014; Yao et al., 2009). The enhanced detrital magnetite may have diluted the relative percentage of biogenic magnetite in Stage 1 with low sea level (Wang et al., 2023). As sea level rises, the reduced flux of detrital magnetite (Chen et al., 2017; Li, Ouyang, et al., 2018) might enhance the previously concealed magnetofossil signals in the northwestern SCS.

In addition, the intermediate water of the SCS, with the lowest oxygen concentration (Li, Rashid, et al., 2018), may result in a relatively anoxic sea-floor environment evidenced by the U and Mo enrichment factors (U_{EF} and Mo_{EF}) (Figure S7 in Supporting Information S1) (Algeo & Tribovillard, 2009). The relatively anoxic environment since the last deglaciation has been conducive to the survival of MTB. The deep-water temperature might increase during the Stage 1 and remained relatively stable during the Stage 2 inferred from the benthic foraminifera $\delta^{18}O$ (Figure 7e) (Lisiecki & Raymo, 2005; Wan & Jian, 2014; Yang et al., 2020). The possibly stable and higher bottom water temperature during Stage 2 might be suitable for the proliferation of MTB, resulting in increased production of magnetofossils. In particular, the needle-shaped giant magnetofossil, which has often been identified in sediments deposited during global hyperthermal events (Chang et al., 2012, 2018; Wagner et al., 2021), also existed in our sediment (Figure 2d).

In summary, according to our records, magnetic minerals act as valuable indicators of continent-ocean environmental changes. The extraction and isolation of different magnetic mineral information from sediments in marginal seas can help reconstruct continent-ocean environmental variations.

6. Conclusion

Systematic magnetic studies were conducted on core SCS-02 from northwestern SCS to reconstruct the magnetic response to sea level and monsoon evolution since the last deglaciation. The main conclusions are summarized as follows.

1. The ratio of hematite to goethite concentration (Hm/Gt) was suitable for precipitation reconstruction in the Red River catchment during the Holocene. The summer monsoon precipitation was relatively low during the mid-Holocene and high during the early- and late-Holocene for the Red River catchment, which was consistent with the precipitation trend from Central to South China but was in anti-phase with that of Northern China. Changes in the intensity and location of the WPSH may be the dominant controller of the Holocene ASM precipitation variation in the Red River catchment.
2. A decoupling between the degree of chemical weathering and ASM was found in the Red River catchment, characterized by a higher chemical weathering degree during the deglaciation than in the Holocene, which may be attributed to the further weathering of exposed shelf materials during the last deglaciation. Pedogenesis on the exposed shelf during the deglaciation produced more fine-grained magnetite.
3. The biogenic magnetite (magnetofossils) content of core SCS-02 was controlled by sea level and deep-water environments. The relatively high abundance of magnetofossils since ∼8 ka BP may be attributed to reduced terrestrial magnetic particle input caused by higher sea levels and possible deep-water environment changes.

Data Availability Statement

Data to support this article are deposited in Zenodo (Sun, 2023).

Acknowledgments
The authors thank two anonymous reviewers for their helpful and constructive reviews of this manuscript. This research was funded by the National Natural Science Foundation of China (42274089 and 42121005), the Science and Technology Innovation Project of Laoshan Laboratory (LSKJ202204400) and the Fundamental Research Funds for the Central Universities (202072001, 202341003), Outstanding Youth Fund of Shandong Province (ZR2022JQ16), the National Program on Global Change and Air-Sea Interaction (Phase II) (GASI-01-WIND-CJ02), and Taishan Scholars (tsqn202306112, ts20190918, tstp20221112).

References

Abrajevitch, A., & Kodama, K. (2011). Diagenetic sensitivity of paleoenvironmental proxies: A rock magnetic study of Australian continental margin sediments. *Geochemistry, Geophysics, Geosystems*, *12*(5), Q05Z24. https://doi.org/10.1029/2010gc003481

Algeo, T. J., & Tribovillard, N. (2009). Environmental analysis of paleoceanographic systems based on molybdenum-uranium covariation. *Chemical Geology*, *268*(3–4), 211–225. https://doi.org/10.1016/j.chemgeo.2009.09.001

Ao, H., Rohling, E. J., Stringer, C., Roberts, A. P., Dekkers, M. J., Dupont-Nivet, G., et al. (2020). Two-stage mid-Brunhes climate transition and mid-Pleistocene human diversification. *Earth-Science Reviews*, *210*, 103354. https://doi.org/10.1016/j.earscirev.2020.103354

Balsam, W., Ji, J., & Chen, J. (2004). Climatic interpretation of the Luochuan and Lingtai loess sections, China, based on changing iron oxide mineralogy and magnetic susceptibility. *Earth and Planetary Science Letters*, *223*(3), 335–348. https://doi.org/10.1016/j.epsl.2004.04.023

Berger, A., & Loutre, M. F. (1991). Insolation values for the climate of the last 10 million years. *Quaternary Science Reviews*, *10*(4), 297–317. https://doi.org/10.1016/0277-3791(91)90033-Q

Chang, L., Harrison, R. J., Zeng, F., Berndt, T. A., Roberts, A. P., Heslop, D., & Zhao, X. (2018). Coupled microbial bloom and oxygenation decline recorded by magnetofossils during the Palaeocene-Eocene thermal maximum. *Nature Communications*, *9*(1), 4007. https://doi.org/10.1038/s41467-018-06472-y

Chang, L., Heslop, D., Roberts, A. P., Rey, D., & Mohamed, K. J. (2016). Discrimination of biogenic and detrital magnetite through a double verwey transition temperature. *Journal of Geophysical Research: Solid Earth*, *121*(1), 3–14. https://doi.org/10.1002/2015JB012485

Chang, L., Roberts, A. P., Williams, W., Fitz Gerald, J. D., Larrasoaña, J. C., Jovane, L., & Muxworthy, A. R. (2012). Giant magnetofossils and hyperthermal events. *Earth and Planetary Science Letters*, *351–352*, 258–269. https://doi.org/10.1016/j.epsl.2012.07.031

Chen, F., Chen, X., Chen, J., Zhou, A., Wu, D., Tang, L., et al. (2014). Holocene vegetation history, precipitation changes and Indian Summer Monsoon evolution documented from sediments of Xingyun Lake, South-west China. *Journal of Quaternary Science*, *29*(7), 661–674. https://doi.org/10.1002/jqs.2735

Chen, Q., Kissel, C., & Liu, Z. (2017). Late Quaternary climatic forcing on the terrigenous supply in the northern South China Sea: Input from magnetic studies. *Earth and Planetary Science Letters*, *471*, 160–171. https://doi.org/10.1016/j.epsl.2017.04.047

Clark, P. U., Shakun, J. D., Baker, P. A., Bartlein, P. J., Brewer, S., Brook, E., et al. (2012). Global climate evolution during the last deglaciation. *Proceedings of the National Academy of Sciences*, *109*(19), E1134–E1142. https://doi.org/10.1073/pnas.1116619109

Clift, P. D. (2006). Controls on the erosion of Cenozoic Asia and the flux of clastic sediment to the ocean. *Earth and Planetary Science Letters*, *241*(3–4), 571–580. https://doi.org/10.1016/j.epsl.2005.11.028

Deng, K., Yang, S., & Guo, Y. (2022). A global temperature control of silicate weathering intensity. *Nature Communications*, *13*(1), 1781. https://doi.org/10.1038/s41467-022-29415-0

Dykoski, C., Edwards, R., Cheng, H., Yuan, D., Cai, Y., Zhang, M., et al. (2005). A high-resolution, absolute-dated Holocene and deglacial Asian monsoon record from Dongge Cave, China. *Earth and Planetary Science Letters*, *233*(1–2), 71–86. https://doi.org/10.1016/j.epsl.2005.01.036

Egli, R., Chen, A. P., Winklhofer, M., Kodama, K. P., & Horng, C.-S. (2010). Detection of noninteracting single domain particles using first-order reversal curve diagrams. *Geochemistry, Geophysics, Geosystems*, *11*(1), Q01Z11. https://doi.org/10.1029/2009GC002916

Gao, J., Wu, G., & Ya, H. (2017). Review of the circulation in the Beibu Gulf, South China sea. *Continental Shelf Research*, *138*, 106–119. https://doi.org/10.1016/j.csr.2017.02.009

Harrison, R. J., & Feinberg, J. M. (2008). FORCinel: An improved algorithm for calculating first-order reversal curve distributions using locally weighted regression smoothing. *Geochemistry, Geophysics, Geosystems*, *9*(5), Q05016. https://doi.org/10.1029/2008GC001987

Harrison, R. J., Muraszko, J., Heslop, D., Lascu, I., Muxworthy, A. R., & Roberts, A. P. (2018). An improved algorithm for unmixing first-order reversal curve diagrams using principal component analysis. *Geochemistry, Geophysics, Geosystems*, *19*(5), 1595–1610. https://doi.org/10.1029/2018GC007511

Haug, G. H., Hughen, K. A., Sigman, D. M., Peterson, L. C., & Rohl, U. (2001). Southward migration of the intertropical convergence zone through the Holocene. *Science*, *293*(5533), 1304–1308. https://doi.org/10.1126/science.1059725

He, K., & Pan, Y. (2020). Magnetofossil abundance and diversity as paleoenvironmental proxies: A case study from southwest Iberian margin sediments. *Geophysical Research Letters*, *47*(8), e2020GL087165. https://doi.org/10.1029/2020GL087165

Hu, D., Böning, P., Köhler, C. M., Hillier, S., Pressling, N., Wan, S., et al. (2012). Deep sea records of the continental weathering and erosion response to East Asian monsoon intensification since 14ka in the South China Sea. *Chemical Geology*, *326–327*, 1–18. https://doi.org/10.1016/j.chemgeo.2012.07.024

Huang, J., Wan, S., Xiong, Z., Zhao, D., Liu, X., Li, A., & Li, T. (2016). Geochemical records of Taiwan-sourced sediments in the South China Sea linked to Holocene climate changes. *Palaeogeography, Palaeoclimatology, Palaeoecology*, *441*, 871–881. https://doi.org/10.1016/j.palaeo.2015.10.036

Jiang, Z., Liu, Q., Roberts, A. P., Dekkers, M. J., Barrón, V., Torrent, J., & Li, S. (2022). The magnetic and color reflectance properties of hematite: From Earth to Mars. *Reviews of Geophysics*, *60*(1), e2020RG000698. https://doi.org/10.1029/2020RG000698

King, J. W., & Channell, J. E. T. (1991). Sedimentary magnetism, environmental magnetism, and magnetostratigraphy. *Reviews of Geophysics*, *29*(S1), 358–370. https://doi.org/10.1002/rog.1991.29.s1.358

Kissel, C., Laj, C., Jian, Z., Wang, P., Wandres, C., & Rebolledo-Vieyra, M. (2020). Past environmental and circulation changes in the South China Sea: Input from the magnetic properties of deep-sea sediments. *Quaternary Science Reviews*, *236*, 106263. https://doi.org/10.1016/j.quascirev.2020.106263

Kissel, C., Liu, Z., Li, J., & Wandres, C. (2016). Magnetic minerals in three Asian rivers draining into the South China sea: Pearl, red, and Mekong rivers. *Geochemistry, Geophysics, Geosystems*, *17*(5), 1678–1693. https://doi.org/10.1002/2016gc006283

Koutavas, A., & Joanides, S. (2012). El Niño-southern oscillation extrema in the Holocene and last glacial maximum. *Paleoceanography*, *27*(4), PA4208. https://doi.org/10.1029/2012PA002378

Lambeck, K., Rouby, H., Purcell, A., Sun, Y., & Sambridge, M. (2014). Sea level and global ice volumes from the last glacial maximum to the Holocene. *Proceedings of the National Academy of Sciences*, *111*(43), 15296–15303. https://doi.org/10.1073/pnas.1411762111

Lascu, I., Harrison, R. J., Li, Y., Muraszko, J. R., Channell, J. E. T., Piotrowski, A. M., & Hodell, D. A. (2015). Magnetic unmixing of first-order reversal curve diagrams using principal component analysis. *Geochemistry, Geophysics, Geosystems*, *16*(9), 2900–2915. https://doi.org/10.1002/2015GC005909

Le, T. P. Q., Garnier, J., Gilles, B., Sylvain, T., & Van Minh, C. (2007). The changing flow regime and sediment load of the Red River, Viet Nam. *Journal of Hydrology*, *334*(1–2), 199–214. https://doi.org/10.1016/j.jhydrol.2006.10.020

Lepre, C. J., & Olsen, P. E. (2021). Hematite reconstruction of late Triassic hydroclimate over the Colorado plateau. *Proceedings of the National Academy of Sciences*, *118*(7), e2004343118. https://doi.org/10.1073/pnas.2004343118

Li, G., Rashid, H., Zhong, L., Xu, X., Yan, W., & Chen, Z. (2018). Changes in deep water oxygenation of the South China Sea since the last glacial period. *Geophysical Research Letters*, *45*(17), 9058–9066. https://doi.org/10.1029/2018GL078568

Li, J., Yan, H., Dodson, J., Xu, Q., Sun, A., Cheng, B., et al. (2018). Regional-scale precipitation anomalies in northern China during the Holocene and possible impact on prehistoric demographic changes. *Geophysical Research Letters*, *45*(22), 12477–12486. https://doi.org/10.1029/2018GL078873

Li, M., Ouyang, T., Roberts, A. P., Heslop, D., Zhu, Z., Zhao, X., et al. (2018). Influence of sea level change and centennial East Asian monsoon variations on northern South China Sea sediments over the past 36 kyr. *Geochemistry, Geophysics, Geosystems*, *19*(5), 1674–1689. https://doi.org/10.1029/2017GC007321

Li, M., Ouyang, T., Zhu, Z., Tian, C., Peng, S., Zhong, H., et al. (2022). Reconstruction of chemical weathering intensity and Asian Summer Monsoon evolution in the Red River basin over the past 36 kyr. *Paleoceanography and Paleoclimatology*, *37*(5), e2021PA004397. https://doi.org/10.1029/2021PA004397

Li, Q., Sun, Q., Xie, M., Ling, Y., Zhu, Z., Zhu, Q.-Z., et al. (2023). Coupled temperature variations in the Huguangyan Maar Lake between high and low latitude. *Quaternary Science Reviews*, *305*, 108011. https://doi.org/10.1016/j.quascirev.2023.108011

Lisiecki, L. E., & Raymo, M. E. (2005). A Pliocene-Pleistocene stack of 57 globally distributed benthic $\delta^{18}O$ records. *Paleoceanography*, *20*(1), PA1003. https://doi.org/10.1029/2004PA001071

Liu, J., Chen, J., Zhang, X., Li, Y., Rao, Z., & Chen, F. (2015). Holocene East Asian summer monsoon records in northern China and their inconsistency with Chinese stalagmite $\delta^{18}O$ records. *Earth-Science Reviews*, *148*, 194–208. https://doi.org/10.1016/j.earscirev.2015.06.004

Liu, Q., Jackson, M. J., Yu, Y., Chen, F., Deng, C., & Zhu, R. (2004). Grain size distribution of pedogenic magnetic particles in Chinese loess/paleosols. *Geophysical Research Letters*, *31*(22), L22603. https://doi.org/10.1029/2004GL021090

Liu, Q., Roberts, A. P., Larrasoaña, J. C., Banerjee, S. K., Guyodo, Y., Tauxe, L., & Oldfield, F. (2012). Environmental magnetism: Principles and applications. *Reviews of Geophysics*, *50*(4), RG4002. https://doi.org/10.1029/2012RG000393

Liu, Z., Zhao, Y., Colin, C., Stattegger, K., Wiesner, M. G., Huh, C.-A., et al. (2016). Source-to-sink transport processes of fluvial sediments in the South China Sea. *Earth-Science Reviews*, *153*, 238–273. https://doi.org/10.1016/j.earscirev.2015.08.005

Long, X., Ji, J., Barrón, V., & Torrent, J. (2016). Climatic thresholds for pedogenic iron oxides under aerobic conditions: Processes and their significance in paleoclimate reconstruction. *Quaternary Science Reviews*, *150*, 264–277. https://doi.org/10.1016/j.quascirev.2016.08.031

Lu, H., Yi, S., Liu, Z., Mason, J. A., Jiang, D., Cheng, J., et al. (2013). Variation of East Asian monsoon precipitation during the past 21 k.y. and potential CO_2 forcing. *Geology*, *41*(9), 1023–1026. https://doi.org/10.1130/G34488.1

McLennan, S. M. (1993). Weathering and global denudation. *The Journal of Geology*, *101*(2), 295–303. https://doi.org/10.1086/648222

Nesbitt, H. W., & Young, G. M. (1982). Early Proterozoic climates and plate motions inferred from major element chemistry of lutites. *Nature*, *299*(5885), 715–717. https://doi.org/10.1038/299715a0

Nguyen, T. T. H., Zhang, W., Li, Z., Li, J., Ge, C., Liu, J., et al. (2016). Magnetic properties of sediments of the Red River: Effect of sorting on the source-to-sink pathway and its implications for environmental reconstruction. *Geochemistry, Geophysics, Geosystems*, *17*(2), 270–281. https://doi.org/10.1002/2015GC006089

Pike, C. R., Roberts, A. P., & Verosub, K. L. (2001). First-order reversal curve diagrams and thermal relaxation effects in magnetic particles. *Geophysical Journal International*, *145*(3), 721–730. https://doi.org/10.1046/j.0956-540x.2001.01419.x

Rao, Z., Li, Y., Zhang, J., Jia, G., & Chen, F. (2016). Investigating the long-term palaeoclimatic controls on the δD and $\delta^{18}O$ of precipitation during the Holocene in the Indian and East Asian monsoonal regions. *Earth-Science Reviews*, *159*, 292–305. https://doi.org/10.1016/j.earscirev.2016.06.007

Roberts, A. P., Florindo, F., Villa, G., Chang, L., Jovane, L., Bohaty, S. M., et al. (2011). Magnetotactic bacterial abundance in pelagic marine environments is limited by organic carbon flux and availability of dissolved iron. *Earth and Planetary Science Letters*, *310*(3–4), 441–452. https://doi.org/10.1016/j.epsl.2011.08.011

Roberts, A. P., Pike, C. R., & Verosub, K. L. (2000). First-order reversal curve diagrams: A new tool for characterizing the magnetic properties of natural samples. *Journal of Geophysical Research*, *105*(B12), 28461–28475. https://doi.org/10.1029/2000JB900326

Roberts, A. P., Zhao, X., Harrison, R. J., Heslop, D., Muxworthy, A. R., Rowan, C. J., et al. (2018). Signatures of reductive magnetic mineral diagenesis from unmixing of first-order reversal curves. *Journal of Geophysical Research: Solid Earth*, *123*(6), 4500–4522. https://doi.org/10.1029/2018JB015706

Scheinost, A. C., Chavernas, A., Barron, V., & Torrent, J. (1998). Use and limitations of second-derivative diffuse reflectance spectroscopy in the visible to near-infrared range to identify and quantify Fe oxide minerals in soils. *Clays and Clay Minerals*, *46*(5), 528–536. https://doi.org/10.1346/CCMN.1998.0460506

Schwertmann, U. (1993). Relations between iron oxides, soil color, and soil formation. In J. M. Bigham & E. J. Ciolkosz (Eds.), *Soil color* (pp. 51–69). https://doi.org/10.2136/sssaspecpub31.c4

Su, N., Yang, S.-Y., Wang, X.-D., Bi, L., & Yang, C.-F. (2015). Magnetic parameters indicate the intensity of chemical weathering developed on igneous rocks in China. *Catena*, *133*, 328–341. https://doi.org/10.1016/j.catena.2015.06.003

Sun, Q. (2023). Data for Millennial-scale precipitation and chemical weathering variations since the last deglaciation recorded by the northwestern South China Sea sediments. [Dataset]. Zenodo. https://doi.org/10.5281/zenodo.8073034

Thompson, R., & Oldfield, F. (1986). *Environmental magnetism* (pp. 28–34). Allen and Unwin. https://doi.org/10.1007/978-94-011-8036-8

Tian, C., Ouyang, T., Li, M., Zhang, J., Peng, S., Zhu, Z., et al. (2020). Magnetic investigation of surface sediments of the northwestern South China Sea: Implication for sediment provenance and transportation. *Journal of Asian Earth Sciences*, *202*, 104530. https://doi.org/10.1016/j.jseaes.2020.104530

Torrent, J., Liu, Q., Bloemendal, J., & Barrón, V. (2007). Magnetic enhancement and iron oxides in the upper Luochuan loess-paleosol sequence, Chinese Loess Plateau. *Soil Science Society of America Journal*, *71*(5), 1570–1578. https://doi.org/10.2136/sssaj2006.0328

Wagner, C. L., Egli, R., Lascu, I., Lippert, P. C., Livi, K. J. T., & Sears, H. B. (2021). In situ magnetic identification of giant, needle-shaped magnetofossils in Paleocene-Eocene Thermal Maximum sediments. *Proceedings of the National Academy of Sciences*, *118*(6), e2018169118. https://doi.org/10.1073/pnas.2018169

Wan, S., Clift, P. D., Zhao, D., Hovius, N., Munhoven, G., France-Lanord, C., et al. (2017). Enhanced silicate weathering of tropical shelf sediments exposed during glacial lowstands: A sink for atmospheric CO_2. *Geochimica et Cosmochimica Acta*, *200*, 123–144. https://doi.org/10.1016/j.gca.2016.12.010

Wan, S., & Jian, Z. (2014). Deep water exchanges between the South China Sea and the Pacific since the last glacial period. *Paleoceanography*, *29*(12), 1162–1178. https://doi.org/10.1002/2013PA002578

Wan, S., Toucanne, S., Clift, P. D., Zhao, D., Bayon, G., Yu, Z., et al. (2015). Human impact overwhelms long-term climate control of weathering and erosion in southwest China. *Geology*, *43*(5), 439–442. https://doi.org/10.1130/G36570.1

Wang, B., Zhong, W., Zhu, C., Ouyang, J., Wei, Z., & Shang, S. (2022). Geochemistry of sediments from a subalpine lake sedimentary succession in the western Nanling mountains, Southern China: Implications for catchment weathering during the last 15400 years. *Chinese Geographical Science*, *32*(3), 537–548. https://doi.org/10.1007/s11769-022-1282-4

Wang, H., Xu, X., Gai, C., Liu, J., Zhong, Y., Jiang, X., et al. (2022). Inverse magnetic fabrics caused by magnetofossils in the northwestern South China Sea since end of the Last Glacial. *Geophysical Research Letters*, *49*(14), e2022GL098507. https://doi.org/10.1029/2022GL098507

Wang, S., Chang, L., Xue, P., Liu, S., Shi, X., Li, J., et al. (2023). Sedimentary modulation of magnetic mineral records in the Central Bengal Fan. *Marine Geology*, *457*, 107010. https://doi.org/10.1016/j.margeo.2023.107010

Wang, X., Chu, G., Sheng, M., Zhang, S., Li, J., Chen, Y., et al. (2016). Millennial-scale Asian summer monsoon variations in South China since the last deglaciation. *Earth and Planetary Science Letters*, *451*, 22–30. https://doi.org/10.1016/j.epsl.2016.07.006

West, A., Galy, A., & Bickle, M. (2005). Tectonic and climatic controls on silicate weathering. *Earth and Planetary Science Letters*, *235*(1–2), 211–228. https://doi.org/10.1016/j.epsl.2005.03.020

White, A. F., & Blum, A. E. (1995). Effects of climate on chemical weathering in watersheds. *Geochimica et Cosmochimica Acta*, *59*(9), 1729–1747. https://doi.org/10.1016/0016-7037(95)00078-E

Xiao, C., Sun, Q., Chen, L., Yin, Z., Chen, L., Guan, Y., et al. (2023). Environmental magnetic characteristics and provenance significance of sediments in NW South China Sea since the past 16 ka. (in Chinese with English Abstract). *Marine Geology and Quaternary Geology*, *43*(1), 13–26. https://doi.org/10.16562/j.cnki.0256-1492.2022091301

Xie, S., Evershed, R. P., Huang, X., Zhu, Z., Pancost, R. D., Meyers, P. A., et al. (2013). Concordant monsoon-driven postglacial hydrological changes in peat and stalagmite records and their impacts on prehistoric cultures in central China. *Geology*, *41*(8), 827–830. https://doi.org/10.1130/G34318.1

Xu, H., Goldsmith, Y., Lan, J., Tan, L., Wang, X., Zhou, X., et al. (2020). Juxtaposition of western Pacific subtropical high on Asian summer monsoon shapes subtropical East Asian precipitation. *Geophysical Research Letters*, *47*(3), e2019GL084705. https://doi.org/10.1029/2019GL084705

Yamazaki, T., Fu, W., Shimono, T., & Usui, Y. (2020). Unmixing biogenic and terrigenous magnetic mineral components in red clay of the Pacific Ocean using principal component analyses of first-order reversal curve diagrams and paleoenvironmental implications. *Earth Planets and Space*, *72*(1), 120. https://doi.org/10.1186/s40623-020-01248-5

Yancheva, G., Nowaczyk, N. R., Mingram, J., Dulski, P., Schettler, G., Negendank, J. F., et al. (2007). Influence of the intertropical convergence zone on the East Asian monsoon. *Nature*, *445*(7123), 74–77. https://doi.org/10.1038/nature05431

Yang, Y., Xiang, R., Zhang, L., Zhong, F., & Zhang, M. (2020). Is the upward release of intermediate ocean heat content a possible engine for low-latitude processes? *Geology*, *48*(6), 579–583. https://doi.org/10.1130/G47271.1

Yao, Y., Harff, J., Meyer, M., & Zhan, W. (2009). Reconstruction of paleocoastlines for the northwestern South China Sea since the last glacial maximum. *Science in China—Series D: Earth Sciences*, *52*(8), 1127–1136. https://doi.org/10.1007/s11430-009-0098-8

Zhang, E., Sun, W., Chang, J., Ning, D., & Shulmeister, J. (2018). Variations of the Indian summer monsoon over the last 30 000 years inferred from a pyrogenic carbon record from south-west China. *Journal of Quaternary Science*, *33*(1), 131–138. https://doi.org/10.1002/jqs.3008

Zhang, M., Smol, J. P., & Bu, Z. (2023). Holocene initiation and expansion of the southern margins of northern peatlands triggered by the East Asian summer monsoon recession. *Geoscience Frontiers*, *14*(2), 101526. https://doi.org/10.1016/j.gsf.2022.101526

Zhang, Q., Roberts, A. P., Ge, S., Liu, Y., Liu, J., Liu, S., et al. (2022). Interpretation of anhysteretic remanent magnetization carriers in magnetofossil-rich marine sediments. *Journal of Geophysical Research: Solid Earth*, *127*(11), e2022JB024432. https://doi.org/10.1029/2022JB024432

Zhang, T., Yang, X., Peng, J., Zhou, Q., Toney, J., Liu, H., & Xie, Y. (2023). Decoupled Indian summer monsoon intensity and effective moisture since the last glaciation in Southwest China. *Geophysical Research Letters*, *50*(10), e2023GL103297. https://doi.org/10.1029/2023GL103297

Zhang, Y., Ji, J., Balsam, W. L., Liu, L., & Chen, J. (2007). High resolution hematite and goethite records from ODP 1143, South China sea: Co-Evolution of monsoonal precipitation and El Niño over the past 600,000 years. *Earth and Planetary Science Letters*, *264*(1–2), 136–150. https://doi.org/10.1016/j.epsl.2007.09.022

Zheng, X., Kao, S., Chen, Z., Menviel, L., Chen, H., Du, Y., et al. (2016). Deepwater circulation variation in the South China Sea since the last glacial maximum. *Geophysical Research Letters*, *43*(16), 8590–8599. https://doi.org/10.1002/2016GL070342

Zhong, W., Xue, J., Zheng, Y., Ouyang, J., Ma, Q., Cai, Y., & Tang, X. (2010). Climatic changes since the last deglaciation inferred from a lacustrine sedimentary sequence in the eastern Nanling Mountains, South China. *Journal of Quaternary Science*, *25*(6), 975–984. https://doi.org/10.1002/jqs.1384

Zhong, Y., Wilson, D. J., Liu, J., Wan, S., Bao, R., Liu, J., et al. (2021). Contrasting sensitivity of weathering proxies to quaternary climate and sea-level fluctuations on the southern slope of the South China Sea. *Geophysical Research Letters*, *48*(24), e2021GL096433. https://doi.org/10.1029/2021GL096433

Zhou, L. P., Oldfield, F., Wintle, A. G., Robinson, S. G., & Wang, J. T. (1990). Partly pedogenic origin of magnetic variations in Chinese loess. *Nature*, *346*(6286), 737–739. https://doi.org/10.1038/346737a0

Zhu, Z., Feinberg, J. M., Xie, S., Bourne, M. D., Huang, C., Hu, C., & Cheng, H. (2017). Holocene ENSO-related cyclic storms recorded by magnetic minerals in speleothems of central China. *Proceedings of the National Academy of Sciences*, *114*(5), 852–857. https://doi.org/10.1073/pnas.1610930114

References From the Supporting Information

Heaton, T. J., Köhler, P., Butzin, M., Bard, E., Reimer, R. W., Austin, W. E. N., et al. (2020). Marine20-The marine radiocarbon age calibration curve (0-55,000 cal BP). *Radiocarbon*, *62*(4), 779–820. https://doi.org/10.1017/RDC.2020.68

Lougheed, B. C., & Obrochta, S. P. (2019). A rapid, deterministic age-depth modeling routine for geological sequences with inherent depth uncertainty. *Paleoceanography and Paleoclimatology*, *34*(1), 122–133. https://doi.org/10.1029/2018PA003457